Influence of Back-Barrier Basin Geometry on Multiple Tidal Inlet Systems
The Roles of Resonance and Bottom Friction

Reef, K.R.G.; Roos, P.C.; Schuttelaars, H. M.; Hulscher, S.J.M.H.

DOI
10.1029/2019JF005261

Publication date
2020

Document Version
Final published version

Published in
Journal of Geophysical Research: Earth Surface

Citation (APA)
Reef, K. R. G., Roos, P. C., Schuttelaars, H. M., & Hulscher, S. J. M. H. (2020). Influence of Back-Barrier Basin Geometry on Multiple Tidal Inlet Systems: The Roles of Resonance and Bottom Friction. *Journal of Geophysical Research: Earth Surface*, *125*(3), 1-20. Article e2019JF005261. https://doi.org/10.1029/2019JF005261

JGR Earth Surface

RESEARCH ARTICLE
10.1029/2019JF005261

Key Points:
- We present a new model for the morphodynamics of multiple inlets connected to a back-barrier basin with an arbitrary plan-view shape
- Local changes in basin width affect the total tidal prism and thus the equilibrium of all inlets, including those further away
- We identify three regimes in how cross-shore basin width affects the equilibrium of inlets: linear, resonant, and dissipative regime

Supporting Information:
- Supporting Information S1

Correspondence to:
K. R. G. Reef,
K.R.G.Reef@utwente.nl

Citation:
Reef, K. R. G., Roos, P. C., Schuttelaars, H. M., & Hulscher, S. J. M. H. (2020). Influence of back-barrier basin geometry on multiple tidal inlet systems: the roles of resonance and bottom friction. *Journal of Geophysical Research: Earth Surface*, *125*, e2019JF005261. https://doi.org/10.1029/2019JF005261

Received 12 JUL 2019
Accepted 16 FEB 2020
Accepted article online 18 FEB 2020

Influence of Back-Barrier Basin Geometry on Multiple Tidal Inlet Systems: The Roles of Resonance and Bottom Friction

K. R. G. Reef[1], P. C. Roos[1], H. M. Schuttelaars[2], and S. J. M. H. Hulscher[1]

[1]Department of Water Engineering and Management, University of Twente, Enschede, The Netherlands, [2]Delft Institute of Applied Mathematics, Delft University of Technology, Delft, The Netherlands

Abstract Observations of barrier coasts around the world suggest that some systems do not conform to the O'Brien-Jarret law. Here we explain this by investigating how resonance and bottom friction affect the response of tidal inlets to variations in basin geometry. Therefore, we develop a morphodynamic barrier coast model that is based on the stability concept of Escoffier for the morphological evolution of the inlets, coupled with an idealized hydrodynamic model that describes the water motion in the outer sea, inlets, and arbitrarily shaped back-barrier basin. We find that the total tidal prism through all inlets is predominantly determined by the (cross-shore) width of the basin and identify three regimes for this. First, a linear regime for narrow basins (i.e., basin width $\ll$ tidal wavelength) where a larger basin leads to a linear increase in total tidal prism. Second, a resonant regime for basins with a width around the resonant condition in which the total tidal prism reaches a peak. This resonance condition is a quarter tidal wavelength for basins without friction, which shifts to narrower basins as friction becomes stronger, down to 0.15 tidal wavelength. Third, a dissipative regime for wide basins (i.e., the cross-shore basin dimension or basin width $\gg$ resonant condition) with sufficiently strong bottom friction in which the total tidal prism does not change for wider basins, because the tidal wave completely dissipates in the basin.

1. Introduction

Barrier coasts, covering around 10% of the worldwide coastline (Glaeser, 1978; Stutz & Pilkey, 2011), are often found near densely populated areas. They are important for their economic, ecologic, touristic value and as protection of the mainland coast (e.g., Oost et al., 2012; Wang et al., 2012). The morphology of barrier coasts changes continuously under the influence of tides, waves, and storms (e.g., Escoffier, 1940; de Swart & Zimmerman, 2009), making them dynamic systems. Following Davis and Hayes (1984), barrier coasts are typically categorized according to the relative dominance of either tides (macro-tidal) or waves (micro-tidal), or equal importance of tides and waves (meso-tidal); this study focuses on the latter two.

An important aspect in the natural evolution of barrier coasts is the evolution of tidal inlets since they are the link between the back-barrier basin and the outer sea. Already in the early 20th century the tidal prism of an inlet was linked to the size of tidal basins, where an almost linear response was observed to differences in basin size between tidal inlets in the United States (O'Brien, 1931; 1969; Jarret, 1976). While these observations showed that a larger tidal basin corresponds to a larger tidal prism (for the same tidal range), the opposite was observed in the Western Dutch Wadden Sea (see Figure 1) after a large bay was closed off, the Zuiderzee in 1932 (e.g., Kragtwijk et al., 2004; Elias et al., 2012). After this closure, the basin width (i.e., cross-shore dimension) was reduced by approximately 60 km, which led to an increase in inlet cross section for the inlets closest to the intervention (e.g., Elias et al., 2012). One suggested explanation (Elias et al., 2012) for this is the shift from a (cross-shore) basin width close to half the tidal wavelength to a basin width closer to quarter wavelength at which resonance occurs (e.g., in the Bay of Fundy). Another example is the Pamlico Sound (NC, USA) where a large back-barrier basin is connected to the outer sea by just three tidal inlets.

The above illustrates that while we have some understanding of how the equilibrium configuration (i.e., size and spacing) of tidal inlets is affected by spatial variations in cross-shore basin geometry, the underlying mechanisms are still not fully understood. The goal of this study is to better explain how tidal inlets are

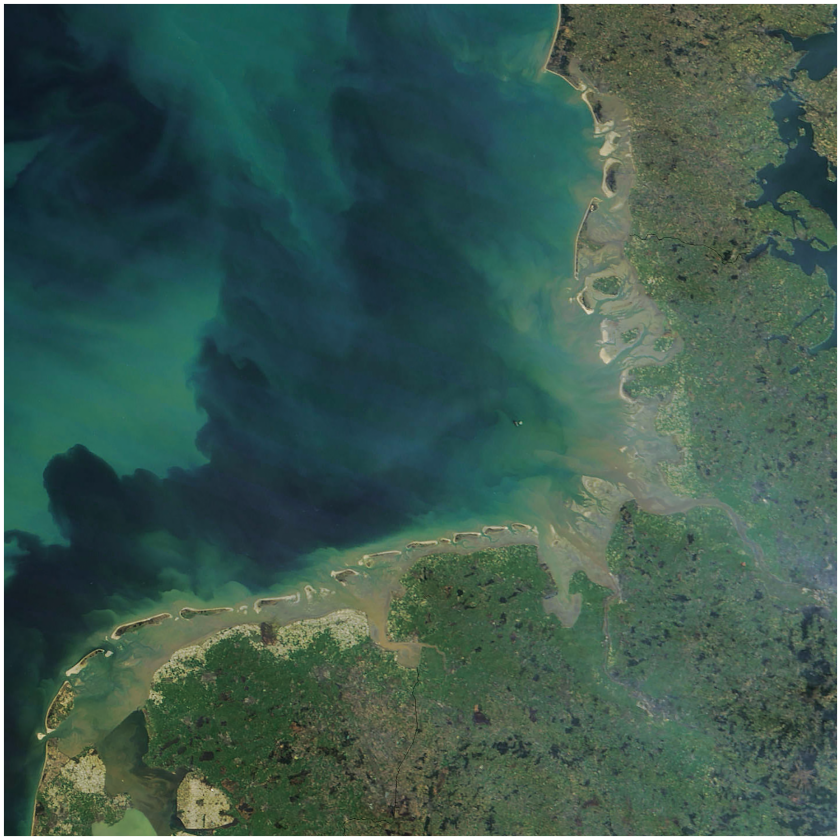

Figure 1. Satellite image of a barrier coast, showing the Dutch, German, and Danish Wadden Sea. Image adapted from NASA.

affected by variations in cross-shore basin geometry and specifically how this is affected by resonance and bottom friction. In particular we aim to answer the following questions:

- How does the cross-shore geometry of the back-barrier basin affect the equilibrium configuration of multiple inlets connected to one back-barrier basin?
- What is the effect of a reduction of the (cross-shore) basin width (e.g., due to human interventions such as damming or land reclamation) on the equilibrium configuration of multiple inlets connected to one back-barrier basin?

To answer our research questions, we extend the idealized barrier coast model of Roos et al. (2013) to allow back-barrier basins of arbitrary shape. We choose an idealized model because it allows us to study the processes affecting multiple inlet systems in isolation and enables us to perform extensive sensitivity analyses. This extension allows us to simulate barrier coast systems with a back-barrier basin of arbitrary plan-view shape, instead of only a single rectangular basin as the model of Roos et al. (2013). Furthermore, the solution method employed results in low computational costs, making this model well suited to cope with the large spatiotemporal scales involved. This choice also allows us to examine a large set of initial inlet conditions, which is essential because initial conditions have been shown to have a large impact on the equilibrium configuration of tidal inlets in process-based models (Dastgheib et al., 2008).

This paper is organized as follows: The model is described in section 2.1 and the solution method in section 2.2. The results are presented in section 3, and the discussion in section 4, followed by the conclusions in section 5.

2. Model and Methods

2.1. Model Formulation

2.1.1. Model Description and Geometry

In our idealized model the morphological evolution of the tidal inlets is governed by the stability concept of Escoffier, and the water motion is described by the linearized shallow water equations, forced by a tidal wave

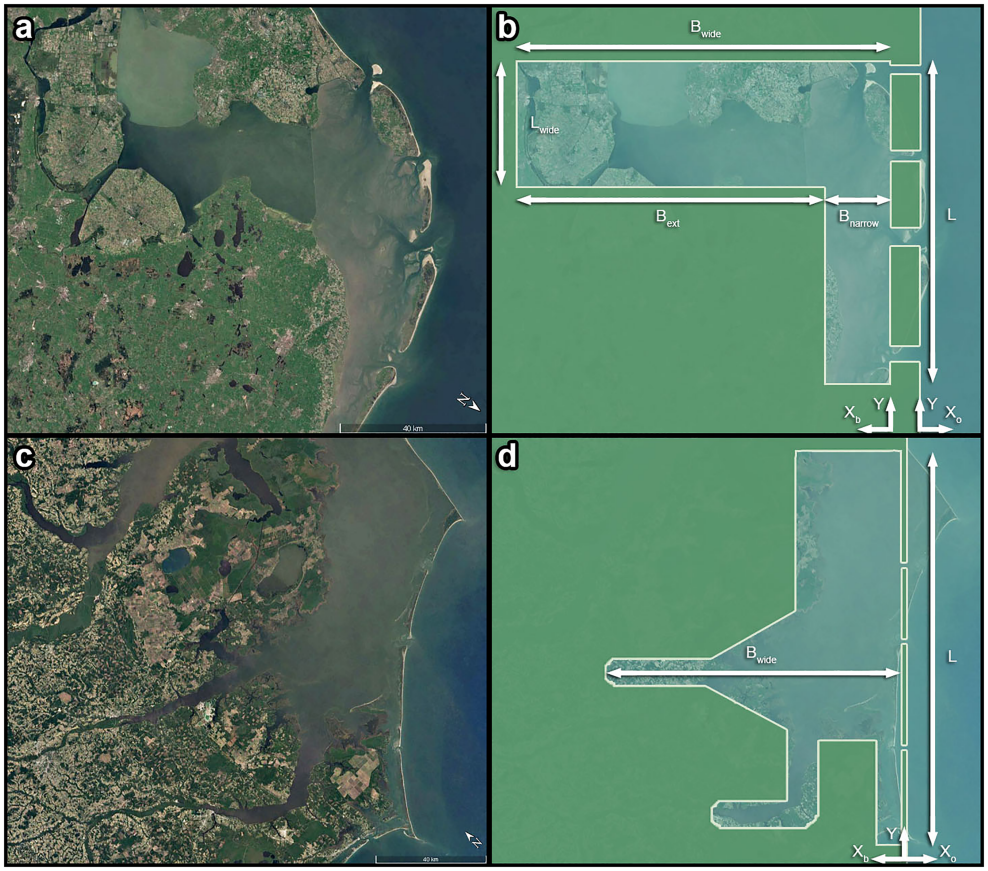

Figure 2. Top row: Satellite image (panel a; Google Earth, 2016) and basin schematization (panel b) for the Western Dutch Wadden Sea. Bottom row: Satellite image (panel c; Google Earth, 2016) and basin schematization (panel d) for the Pamlico Sound (NC, USA). In the left column a length scale and north arrow are provided for reference. In the right column, shown in blue from left to right, are the tidal basin (with a wide and narrow part), the tidal inlets, and the outer sea. Shown in green is the mainland and the barrier islands. Key dimensions such as the (long-shore) basin length L and (cross-shore) basin width B are provided for the entire basin and for different parts of the Wadden Sea basin. The positive x-direction and y-direction for both the basin (x_b & y) and the outer sea (x_o & y) are indicated as well.

on the outer sea. As model domain, we consider a simplified barrier coast consisting of a semi-infinite outer sea bordering a straight coast, interrupted by a set of J tidal inlets that connect the outer sea to an arbitrarily shaped tidal basin (Figure 2) with surface area A_b. Each inlet j is assumed to have a rectangular cross section, with width b_j and depth h_j. The shape of the inlet is fixed using a constant shape factor $\gamma^2 = h_j/b_j$ (e.g., de Swart & Zimmerman, 2009). This implies

$$A_j = b_j h_j = b_j^2 \gamma^2. \tag{1}$$

The domains used in this study are schematizations of two real-world barrier coast systems. The first is a schematization of the Western Dutch Wadden Sea (see Figure 2 top row) consisting of a narrow and wide part (i.e., the top and bottom part in panel b of Figure 2, respectively). The width of this wide part will be varied later on in our analysis. The second is a schematization of the Pamlico Sound, North Carolina (see Figure 2 bottom row), ranging from Cape Lookout to Cape Hatteras and including parts of the Neuss and Pamlico estuaries. The parameter values corresponding to these domains, one set for the Western Dutch Wadden Sea and one for the Pamlico Sound, are given in Table 1.

2.1.2. Morphodynamics

For meso-tidal barrier coasts, both tides and waves are important for the morphological evolution of the tidal inlets (Davis & Hayes, 1984). The tides export sediment from inlet channels leading to erosion, whereas wave-induced littoral drift imports sediment into the inlet channel leading to accretion. Escoffier (1940) argued that an inlet is in equilibrium if the erosion due to the tides and the accretion due to waves balance each other.

Table 1
Parameters Used in This Study

Parameter	Symbol (unit)	Wadden Sea	Pamlico Sound
Tidal elevation amplitude in sea	Z (m)	1	0.325
Tidal frequency in sea	ω (rad/s)	1.405×10^{-4}	1.405×10^{-4}
Long-shore tidal wave number	k_t (rad/m)	0	0
Basin depth	h_b (m)	5	4
Basin length[a]	L (km)	75	135
Wide part basin length[a]	L_w (km)	30	100
Wide part basin width[b]	B_w (km)	20–120	—
Narrow part basin width[b]	B_n (km)	20	—
Drag coefficient	c_d (-)	2.5×10^{-3}	2.5×10^{-3}
Initial inlet depth	h_j (m)	5	5
Inlet length	l_j (km)	5	5
Initial inlet width	b_j (km)	1 ± 0.1[c]	1 ± 0.1[c]
Inlet shape factor	γ^2 (-)	0.005	0.005
Number of initial inlets	J_{init} (-)	50	70
Outer sea depth	h_o (m)	20	20
Sediment import	M (m^3/year)	1×10^6	0.59×10^6
Morphodynamic timestep	Δt (year)	0.5	1
No. of simulations in one ensemble	n (-)	100	—

[a]We define basin length as the long-shore dimension of the basin (see Figure 2). [b]We define basin width as the cross-shore dimension of the basin (see Figure 2). [c]The actual initial width of an inlet is randomized using a uniform distribution between 0.9 and 1.1 km.

In the approach of Escoffier (1940), the sediment export, denoted by X, is modeled as a function of the tidal velocity amplitude U in the inlet. The sediment import denoted by M is parameterized as a function of the equilibrium velocity U_{eq}. If $U < U_{eq}$ the inlet accretes, if $U = U_{eq}$ the inlet is in equilibrium, and if $U > U_{eq}$ it erodes. Using this concept and a simple hydrodynamic model with a spatially uniform water level in the basin, Escoffier (1940) found so-called closure curves describing the potential evolution of a single inlet system (Figure 3). Using these closure curves it is found that either two equilibria (one stable and one unstable), one equilibrium, or no equilibrium at all exists. An equilibrium is stable if after a perturbation of the inlet cross section, it returns to its equilibrium size. More recently, process-based support for this stability concept was provided using complex numerical models (Tran et al., 2012; Nahon et al., 2012).

Escoffier's concept forms the basis of our morphodynamic model governing the evolution of the inlet cross sections. The time evolution of the cross-sectional area A_j of each inlet j is controlled by the volumetric import M (assumed equal for all inlets) and export X_j of sediment that is assumed to be spatially uniform

$$l_j \frac{dA_j}{dt} = X_j - M, \tag{2}$$

with l_j the length of inlet j. The tide-driven export X_j is taken to be proportional to the tidal velocity amplitude in the inlet U_j cubed: $X_j = \kappa U_j^3$, with κ a constant. The wave-driven import M is externally imposed and similar to previous studies (van de Kreeke, 2004; van de Kreeke et al., 2008; Roos et al., 2013) assumed identical for all inlets, implying that all necessary sediment can be supplied by the wave-induced long-shore drift. This results in an effective equilibrium velocity U_{eq} by defining $M = \kappa U_{eq}^3$. Equation (2) is then rewritten as

$$\frac{dA_j}{dt} = \frac{M}{l_j}\left[\left(\frac{U_j}{U_{eq}}\right)^3 - 1\right]. \tag{3}$$

From this equation we can compute the change in cross-sectional area, given the velocity amplitude U_j in the inlet. To find U_j, we use a hydrodynamic model that is in part solved analytically and in part numerically. This hydrodynamic model is presented in the next subsection.

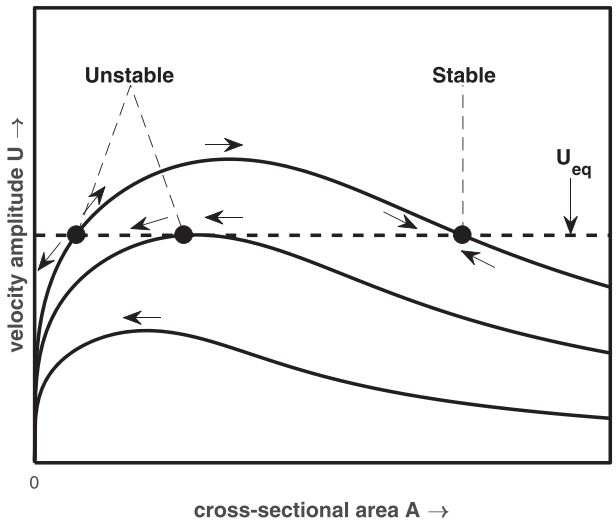

Figure 3. Three closure curves for a single inlet, as presented by Escoffier (1940). Each closure curve shows the inlet's velocity amplitude U as a function of inlet area A. Intersection with an equilibrium velocity U_{eq} (i.e., at $U = U_{eq}$) yields zero, one, or two equilibria. Two equilibria are found if $U > U_{eq}$ for some A, one is found if both coincide, and none are found if $U < U_{eq}$ for all A. In the case of two equilibria one is stable and one is unstable.

2.1.3. Hydrodynamics

The hydrodynamic model simulates the water motion in the outer sea, the tidal inlets, and the tidal basin. It is forced by an M_2-tidal wave in the outer sea resulting in a flow of water through the inlets, which in turn triggers oscillations in the back-barrier basin and in the outer sea. On the coastline of the outer sea and on the basin boundaries, a no-flow boundary condition is prescribed.

To describe the water motion in each inlet j, we consider the linearized cross-sectionally averaged momentum equation, with u_j the cross-sectionally averaged flow velocity that is uniform over the channel length. Furthermore, assuming a constant surface gradient in the inlet, the momentum equation reduces to

$$\frac{\partial u_j}{\partial t} + \frac{r_j u_j}{h_j} = -g\frac{\langle \eta_o \rangle_j - \langle \eta_b \rangle_j}{l_j}, \tag{4}$$

with h_j the inlet depth, η_o the water level in the outer sea (denoted by subscript o), and η_b the water level in the tidal basin (denoted by subscript b). The angle brackets denote averaging over the width of a tidal inlet j, located at either $x_o = 0$ or $x_b = 0$ and defined as $\langle \eta_o \rangle_j = b_j^{-1} \int_{y_j - b_j/2}^{y_j + b_j/2} \eta_o(0, y) \mathrm{d}y$, with y_j the centre location of inlet j. Here x_b is the x-direction in the basin (with $x_b = 0$ at the basin side of the inlet) and x_o the x-direction in the outer sea (with $x_o = 0$ at the outer sea side of the inlet); both are shown in Figure 2, together with the y-direction that is the same for the basin and outer sea. Furthermore, in equation (4) the coefficient r_j is a linearized bottom friction coefficient following from Lorentz's linearization (Lorentz, 1922):

$$r_j = \frac{8}{3\pi} c_d U_j, \tag{5}$$

with drag coefficient c_d and velocity scale U_j (see section 2.2.2). The pressure gradient over the inlet channel (ρ times the r.h.s. of equation (4)) is due to the difference in elevation between the outer sea $\langle \eta_o \rangle_j$ and the basin $\langle \eta_b \rangle_j$, both averaged over the inlet width, with $g = 9.81$ m s^{-2} the gravitational acceleration.

Since our model equations are linearized, the elevation at the open sea $\eta_o(t, x_o, y)$ can be decomposed in an elevation related to the incoming tidal wave (i.e., $Z\cos(\omega t + k_t y)$, the tidal elevation that forces the entire system) and contributions from each inlet $\eta_{o,j}(t, x_o, y)$ due to radiating waves

$$\eta_o(t, x_o, y) = Z\cos(\omega t + k_t y) + \sum_{j=1}^{J} \eta_{o,j}(t, x_o, y), \tag{6}$$

with k_t the long-shore component of the wave number of the incoming tide and ω the angular/radian frequency of the tide. The elevation in the basin $\eta_b(t, x_b, y)$ is the superposition (again allowed because of linearity) of oscillations $\eta_{b,j}(t, x_b, y)$ due to water flowing through all inlets:

$$\eta_b(t, x_b, y) = \sum_{j=1}^{J} \eta_{b,j}(t, x_b, y). \tag{7}$$

Since the water depth in the outer sea is large and the influence of Coriolis acceleration on the cross-sectional stability of tidal inlets is small (Brouwer et al., 2013), we neglect bottom friction and Coriolis acceleration. The resulting linearized depth-averaged shallow water equations read

$$\frac{\partial \mathbf{u}_o}{\partial t} = -g(\eta_o, \tag{8a}$$

$$\frac{\partial \eta_o}{\partial t} + h_o((\cdot \mathbf{u}_o) = 0, \tag{8b}$$

with h_o the outer sea depth (assumed to be spatially uniform and constant in time), $(= (\partial/\partial x_o, \partial/\partial y)$, and $\mathbf{u}_o = (u_o, v_o)$ the depth-averaged flow velocity with components in the x_o-direction and y-direction, which are indicated in Figure 2. At the outer sea's closed boundaries (i.e., where no inlets are present), we require the normal velocity to vanish, that is

$$u_o = 0, \text{ so} \frac{\partial \eta_o}{\partial x_o} = 0, \quad \text{at} x_o = 0. \tag{9}$$

Furthermore, we only allow radiating waves propagating away from the inlets.

In the basin we include the effect of bottom friction, as the basin is much shallower than the outer sea, but we still neglect Coriolis acceleration. The resulting linearized system of equations reads:

$$\frac{\partial \mathbf{u}_b}{\partial t} + \frac{r_b \mathbf{u}_b}{h_b} = -g(\eta_b, \tag{10a}$$

$$\frac{\partial \eta_b}{\partial t} + h_b((\cdot \mathbf{u}_b) = 0, \tag{10b}$$

with h_b the basin depth (assumed to be spatially uniform and constant in time), $(= (\partial/\partial x_b, \partial/\partial y)$, and $\mathbf{u}_b = (u_b, v_b)$ the depth-averaged flow velocity with components in the x_b-direction (u_b) and y-direction (v_b). The linearized friction coefficient r_b according to Lorentz's linearization (Lorentz, 1922) is

$$r_b = \frac{8}{3\pi} c_d U_b, \tag{11}$$

with U_b the velocity scale in the basin (see section 2.2.2). At the closed boundaries of the tidal basin (i.e., where no inlets are present), we require the normal velocity to vanish

$$\mathbf{u}_b \cdot \mathbf{n} = 0 \text{ so } (\eta_b \cdot \mathbf{n} = 0, \quad \text{at} \quad \partial\Omega, \tag{12}$$

with $\mathbf{n}$ the normal vector at the coastline $\partial\Omega$ where no inlets are present. Finally, at the tidal inlets we require the transport of water through each inlet j to match the transport of water in the adjacent sea and basin, that is

$$h_o\langle u_o\rangle_j = h_j u_j = h_b\langle u_b\rangle_j, \text{for} j \in [1, J], \tag{13}$$

where the angle brackets again denote averaging over the width of a tidal inlet j.

2.2. Outline of Solution Method

In this section we present an outline of the solution method for both the morphodynamic and the hydrodynamic part of the model. The former is solved using a forward Euler discretization of equation (3), with

timestep Δt (given in Table 1). The latter is solved analytically—except for the eigenfunctions in the basin that are found numerically (see Appendices A and B)—and yields flow velocities and water levels in the outer sea, tidal inlets, and basin.

The hydrodynamic part of the model is solved as follows. We first express the variables as a product of a complex amplitude and a time-periodic factor. Next, we express both the water motions in the basin and those in the outer sea in terms of the flow velocities in all inlets (see Appendix A). Combining this with the momentum equation for each inlet yields a system of linear equations for the velocity amplitudes in the inlets. This system of equations is solved numerically using standard techniques.

2.2.1. Expansion of Variables

We first express both the water levels and flow velocities as the product of complex amplitudes (denoted by a hat) and a time-periodic factor

$$(\eta_\mathrm{o}, u_\mathrm{o}, v_\mathrm{o}) = \Re\left\{(\hat{\eta}_\mathrm{o}, \hat{\mathrm{u}}_\mathrm{o}, \hat{\mathrm{v}}_\mathrm{o})\exp(\mathrm{i}\omega t)\right\}, \tag{14}$$

$$(\eta_\mathrm{b}, u_\mathrm{b}, v_\mathrm{b}) = \Re\left\{(\hat{\eta}_\mathrm{b}, \hat{\mathrm{u}}_\mathrm{b}, \hat{\mathrm{v}}_\mathrm{b})\exp(\mathrm{i}\omega t)\right\}, \tag{15}$$

$$u_j = \Re\left\{\hat{\mathrm{u}}_j \exp(\mathrm{i}\omega t)\right\}. \tag{16}$$

Here, $\Re$ means taking the real part and ω is the tidal frequency already introduced in section 2.1.3. Next, by substituting equations (14) to (16) in equations (6) and (7), the momentum equation (equation (4)) for an inlet j_a can be written as

$$\mathrm{i}\omega\mu_{j_\mathrm{a}}^2 \hat{\mathrm{u}}_{j_\mathrm{a}} = -\frac{g}{l_{j_\mathrm{a}}}\left[\underbrace{Z\langle\exp(\mathrm{i}k_\mathrm{o}y)\rangle_{j_\mathrm{a}}}_{\text{(I)}} + \underbrace{\left\langle\sum_{j_\mathrm{s}=1}^{J}\hat{\eta}_{\mathrm{o},j_\mathrm{s}}\right\rangle_{j_\mathrm{a}}}_{\text{(II)}} - \underbrace{\left\langle\sum_{j_\mathrm{s}=1}^{J}\hat{\eta}_{\mathrm{b},j_\mathrm{s}}\right\rangle_{j_\mathrm{a}}}_{\text{(III)}}\right], \tag{17}$$

with $\mu_{j_\mathrm{a}}^2 = 1 - \mathrm{i}r_{j_\mathrm{a}}/(\omega h_{j_\mathrm{a}})$ the frictional correction factor. Equation (17) shows that the flow of water through inlet j_a, $\hat{\mathrm{u}}_{j_\mathrm{a}}$ is affected by all inlets j_s. There are three contributions to $\hat{\mathrm{u}}_{j_\mathrm{a}}$: one is related to the tidal elevation in the outer sea due to the forced tidal wave (Term I), the second contribution is related to waves radiating from the tidal inlets resulting in an additional sea surface elevation at the inlets (Term II), and the third contribution is due to the oscillating water level in the basin (Term III).

To calculate the velocity amplitudes in the inlet, given the tidal wave characteristics, we express the latter two surface elevation contributions (i.e., Terms II and III) in terms of $\hat{\mathrm{u}}_{j_\mathrm{s}}$. To this end we use the so-called sea impedance coefficients $z_{\mathrm{o},j_\mathrm{s},j_\mathrm{a}}$ and basin impedance coefficients $z_{\mathrm{b},j_\mathrm{s},j_\mathrm{a}}$, which follow from the model equations (i.e., equation (10b)). These coefficients provide a relation between the surface elevation amplitude experienced by inlet j_a due to a flow of water through inlet j_s

$$\left\langle\hat{\eta}_{\mathrm{o},j_\mathrm{s}}(0,y)\right\rangle_{j_\mathrm{a}} = z_{\mathrm{o},j_\mathrm{s},j_\mathrm{a}}\hat{\mathrm{u}}_{j_\mathrm{s}}, \tag{18a}$$

$$\left\langle\hat{\eta}_{\mathrm{b},j_\mathrm{s}}(0,y)\right\rangle_{j_\mathrm{a}} = z_{\mathrm{b},j_\mathrm{s},j_\mathrm{a}}\hat{\mathrm{u}}_{j_\mathrm{s}}, \tag{18b}$$

where explicit expressions for the basin impedance coefficients $z_{\mathrm{b},j_\mathrm{s},j_\mathrm{a}}$ and sea impedance coefficients $z_{\mathrm{o},j_\mathrm{s},j_\mathrm{a}}$ are given in Appendix A. Substituting this expression in equation (17) yields

$$\mathrm{i}\omega\mu_{j_\mathrm{a}}^2 \hat{\mathrm{u}}_{j_\mathrm{a}} = -\frac{g}{l_{j_\mathrm{a}}}\left[Z\langle\exp(\mathrm{i}k_\mathrm{o}y)\rangle_{j_\mathrm{a}}\sum_{j=1}^{J} + \sum_{j_\mathrm{s}=1}^{J} z_{\mathrm{o},j_\mathrm{s},j_\mathrm{a}}\hat{\mathrm{u}}_{j_\mathrm{s}} - \sum_{j_\mathrm{s}=1}^{J} z_{\mathrm{b},j_\mathrm{s},j_\mathrm{a}}\hat{\mathrm{u}}_{j_\mathrm{s}}\right], \tag{19}$$

resulting in a linear system of equations for the velocity amplitudes $\hat{\mathrm{u}}_j$ that is solved numerically using standard techniques.

2.2.2. Velocity Scales for the Friction Formulation

The velocity scales U_b and U_j, as used in the friction coefficients r_b and r_j (equations (5) and 12) and defined as

$$U_b = \sqrt{\frac{1}{A_b}\iint_{A_b}\left(|\hat{u}_b|^2 + |\hat{v}_b|^2\right) dx_b\, dy} \quad \text{and} \quad U_j = |\hat{u}_j|. \tag{20}$$

will be determined iteratively since they are both model input and output. First, an initial guess is used as input. Next, the velocity scales are updated iteratively by applying an underrelaxation procedure until the relative difference between the two is below an error tolerance threshold of 10^{-10}.

2.3. Design of Model Experiments

2.3.1. Single Simulation

In each simulation, we start with a so-called oversaturated coast containing J_{init} equidistantly spaced tidal inlets and simulate the morphologic evolution of the inlets. We slightly randomize the initial width (up to ±10% from the value in Table 1) of all tidal inlets in each simulation, allowing for possible different equilibrium configurations to be found. The simulation spans 1,000 years, a period that is large enough for the system to reach an equilibrium (or near-equilibrium) configuration. The model results consist of the inlet cross-sections A_j; the tidal elevation amplitude in the basin $\hat{\eta}_b$ and outer sea $\hat{\eta}_o$; and the tidal velocity amplitude in the basin $\mathbf{u}_b$, inlet $\hat{u}_j$, and outer sea $\mathbf{u}_o$.

To demonstrate that our model is capable of simulating various barrier coast systems, we perform three representative model runs, two for Wadden Sea parameters and one for Pamlico Sound parameters (see Table 1). For the Wadden Sea parameters, we consider both the present-day system in which $B_w = 30$ km and the former system (i.e., pre-closure) in which $B_w = 120$ km. Since the Western Dutch Wadden Sea is a meso-tidal barrier coast with drumstick shape barrier islands and four tidal inlets (although up to 10 have been open in the last two millennia, see Vos & Knol, 2015), we expect our model to simulate multiple inlets and barrier islands with limited lengths (i.e., long-shore direction). Since the Pamlico Sound is a micro-tidal barrier coast with very long and thin barrier islands and three tidal inlets (although multiple inlets have opened and closed of the past two millennia, see Mallinson et al., 2018), we expect our model to simulate a small number of inlets and thus very long barrier islands.

2.3.2. Ensemble Simulation

To study the effect of basin geometry on the size and spacing of tidal inlets, we performed a sensitivity analysis by varying the basin width (i.e., the cross-shore dimension) in the Wadden Sea inspired domain (i.e., shown in the top row of Figure 4). For this sensitivity analysis, we use 21 ensembles in which the width of the back-barrier basin in the wide part of the basin B_w is varied from 20 km (i.e., $B_w = B_n$) to 120 km (the maximum extent of the Western Dutch Wadden Sea before closure of the Zuiderzee). Each ensemble consists of 100 simulations, using the Wadden Sea parameters and the same set of 100 randomized inlet widths for all ensembles, to ensure that variations in equilibrium configurations are solely due to changes in basin geometry.

Two types of experiments are carried out. The first set of experiments is used to investigate to what extent the geometry in one part of the basin affects the equilibrium configuration of tidal inlets in other parts of the basin. To this end, we kept the width in the narrow part of the basin B_n constant, while varying B_w. These experiments are referred to as *fixed-geometry runs*.

The second set of experiments is used to study the effect of basin reduction on the equilibrium configuration of tidal inlets. In these experiments, we first consider a wide tidal basin ($B_w = 120$ km). After 500 years (i.e., halfway the simulation) the basin width is reduced in the wide part of the basin, this reduction varies from 5 to 100 km. With this set of experiments, we simulate how the equilibrium configuration of tidal inlets changes due to an intervention, instead of finding the equilibrium state that an initially oversaturated coast will reach. These experiments are referred to as *intervention runs*.

We analyze the results of each model run by determining three metrics for the total basin (denoted by a subscript t): the ratio of the inlet cross sections and its initial size $A_j/A_{init,j}$ for all open inlets j, all in the total basin (i.e., $A_{j,all}/A_{init,j,all}$), the number of open inlets J_t, and the dimensionless total tidal prism $P_t/P_{ref,t}$, with

$$P_t = \sum_{j=1}^{J} \frac{2|\hat{u}_j|}{\omega} A_j, \quad \text{and} \quad P_{ref,t} = ZA_{ref\ basin}. \tag{21}$$

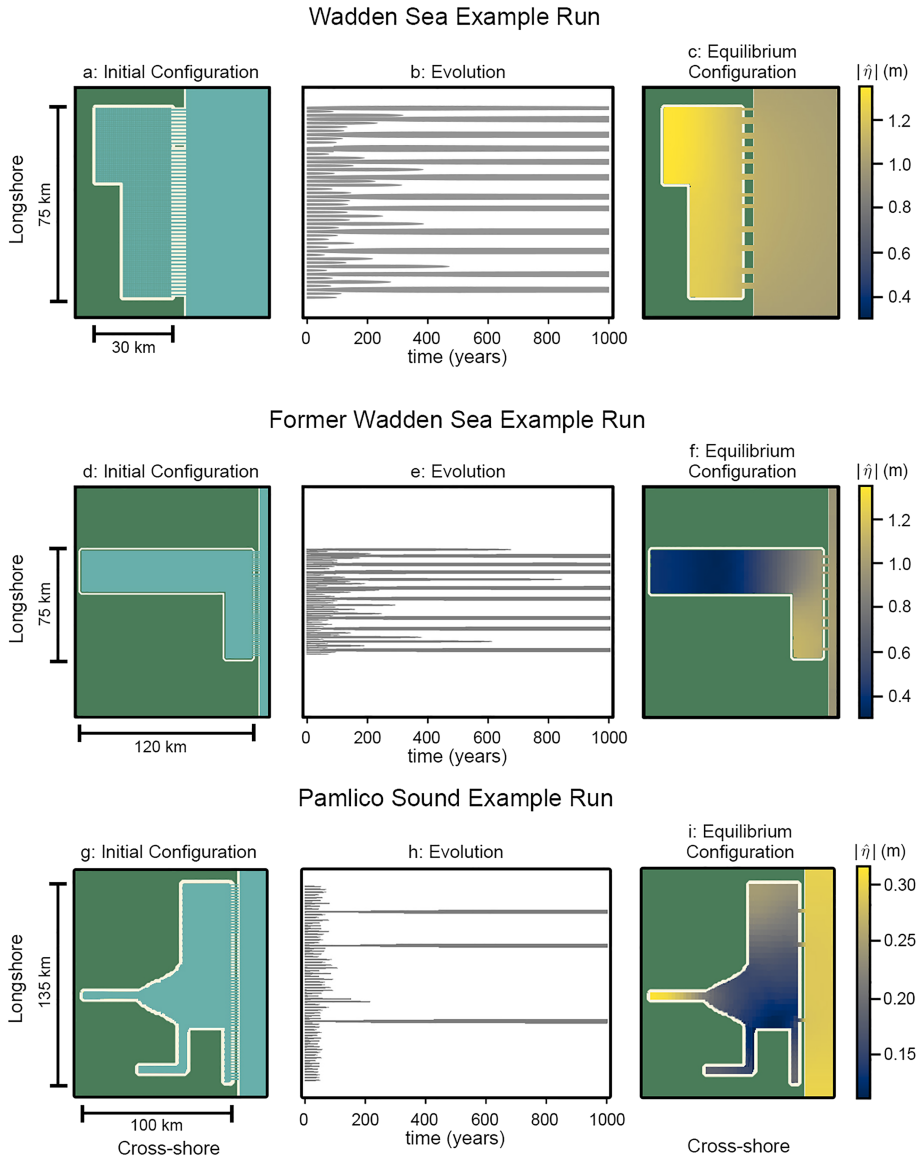

Figure 4. Three example runs for the present Wadden Sea domain (top row, with $B_w = 30$ km), the former Wadden Sea (middle row, with $B_w = 120$ km), and the Pamlico Sound domain (bottom row). Panels a, d, and g show the initial oversaturated barrier coast (top view); panels b, e, and h, the evolution of the tidal inlets (time stack); panels c, f, and i, the equilibrium configuration (top view).

Here $A_{\text{ref basin}}$ is the basin surface area. Since we vary the basin area of the Wadden Sea basin, we choose one reference basin area $A_{\text{ref basin}}$ that is equal to the basin area of the smallest Wadden Sea basin that we consider in this study (i.e., for which $B_w = B_n = 20$ km). Similarly, these metrics can be defined for the wide and narrow part of the Wadden Sea basin, by replacing the total quantities by quantities for the wide part of the basin ($A_{j,w}/A_{\text{init},j,w}$, J_w, and $P_w/P_{\text{ref},w}$ with $P_{\text{ref},w} = ZL_wB_n$) and the narrow part of the basin ($A_{j,n}/A_{\text{init},j,n}$, J_n, and $P_n/P_{\text{ref},n}$ with $P_{\text{ref},n} = Z(L - L_w)B_n$). Per ensemble we aggregate the three metrics and determine the median, 50% envelope, and 100% envelope for each basin configuration.

3. Results

3.1. Representative Model Runs

Here we present the results of three representative model runs (using both the Wadden Sea and Pamlico Sound parameters from Table 1). These representative model runs are individual realizations from the ensembles described in section 2.3.2. Figure 4 shows the initial configuration (panels a, d, and g), evolution

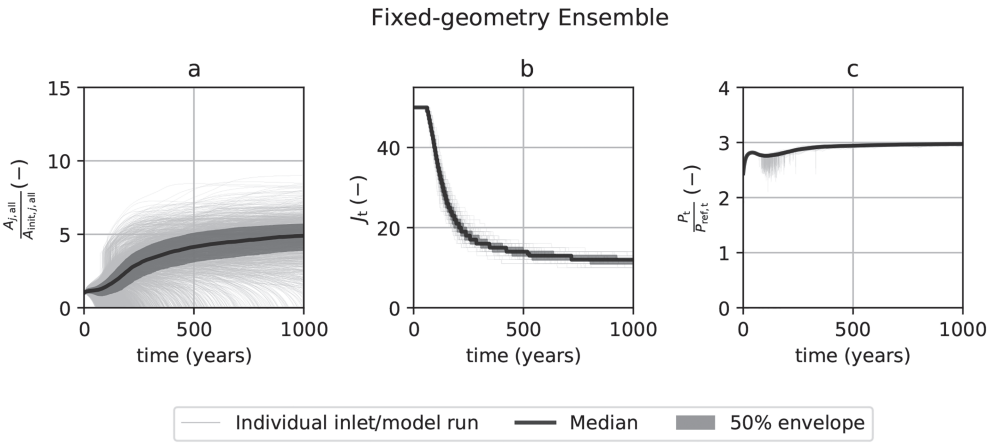

Figure 5. Results of a single ensemble run (for $B_w = 30$ km; i.e., the same basin as the example run) in three metrics: (a) the relative inlet size $A_{j,all}/A_{init,j,all}$ of all open inlets; (b) the number of inlets J_t; (c) the dimensionless tidal prism $P_t/P_{ref,t}$ (see section 2.3.1). These are plotted for the entire duration of the simulation.

(panels b, e, and h), and equilibrium configuration (panels c, f, and i) of the tidal inlets. In the present-day Wadden Sea simulation (top row), the initially oversaturated barrier coast ($J_{init} = 50$) evolved into an equilibrium state where in this example only 12 inlets remain open and 38 have closed. In the former Wadden Sea simulation (middle row), the initially oversaturated barrier coast ($J_{init} = 50$) evolved into an equilibrium state where in this example only eight inlets remained open and 42 have closed. In the Pamlico Sound simulation (bottom row), the initially oversaturated barrier coast ($J_{init} = 70$) evolved into an equilibrium state where in this example only three inlets remain open and 67 have closed.

Comparison of the present-day Wadden Sea example run (Figure 4 top row) with the real-world system (Elias et al., 2012) reveals that our model correctly simulates a slight increase in tidal amplitude near the back of the basin. Regarding the tidal inlets, our model underestimates the inlet cross sections and overestimates the number of inlets that remain open, in turn leading to simulated barrier islands that are shorter than those currently present in the Western Dutch Wadden Sea. For the former Wadden Sea example run (Figure 4 middle row), a comparison with observations from the past (State Committee on the Zuiderzee, 1926) shows that our model correctly simulates a decrease in tidal amplitude as the basin extends further. For the former Wadden Sea domain, our model appears to predict a number of inlets and barrier island lengths that are in the same range as found in reconstructed paleographic maps (Oost et al., 2012; Vos & Knol, 2015; de Haas et al., 2018). The simulated number of inlets is slightly larger than the number of inlets currently present in the Western Dutch Wadden Sea.

Comparison of the example Pamlico Sound model run (Figure 4 bottom row) with the real-world system (Inman & Dolan, 1989; United States Geological Survery, 2019; National Oceanic and Atmospheric Administration, 2020) reveals that our model correctly simulates the tidal amplitude pattern (i.e., lower in the basin and higher on the Pamlico river) and the number of inlets and barrier island lengths (although these results slightly vary for different initial conditions) but overestimates their total cross section. Finally, the time period over which the inlets reach a stable equilibrium differs per example run. For the present-day Wadden Sea, this period ranges from 100 to 500 year, for the former Wadden Sea, this period ranges from 100 to 800 year, and for the Pamlico Sound, this period ranges from 50 to 250 year.

3.2. Fixed-Geometry Runs

The experiments for the fixed-geometry runs consist of 21 ensembles of 100 model runs each. For the ensemble corresponding to the basin of the example run where $B_w = 30$ km, the evolution of the ratio $A_{j,all}/A_{init,j,all}$ for each open inlet j in the total basin (panel a), the number of inlets J_t (panel b), and dimensionless tidal prism $P_t/P_{ref,t}$ (panel c) are shown are shown in Figure 5.

The first panel shows that the inlets that remain open are approximately five times larger than their initial size. The second panel shows that the number of inlets reaches its equilibrium value right before the end of

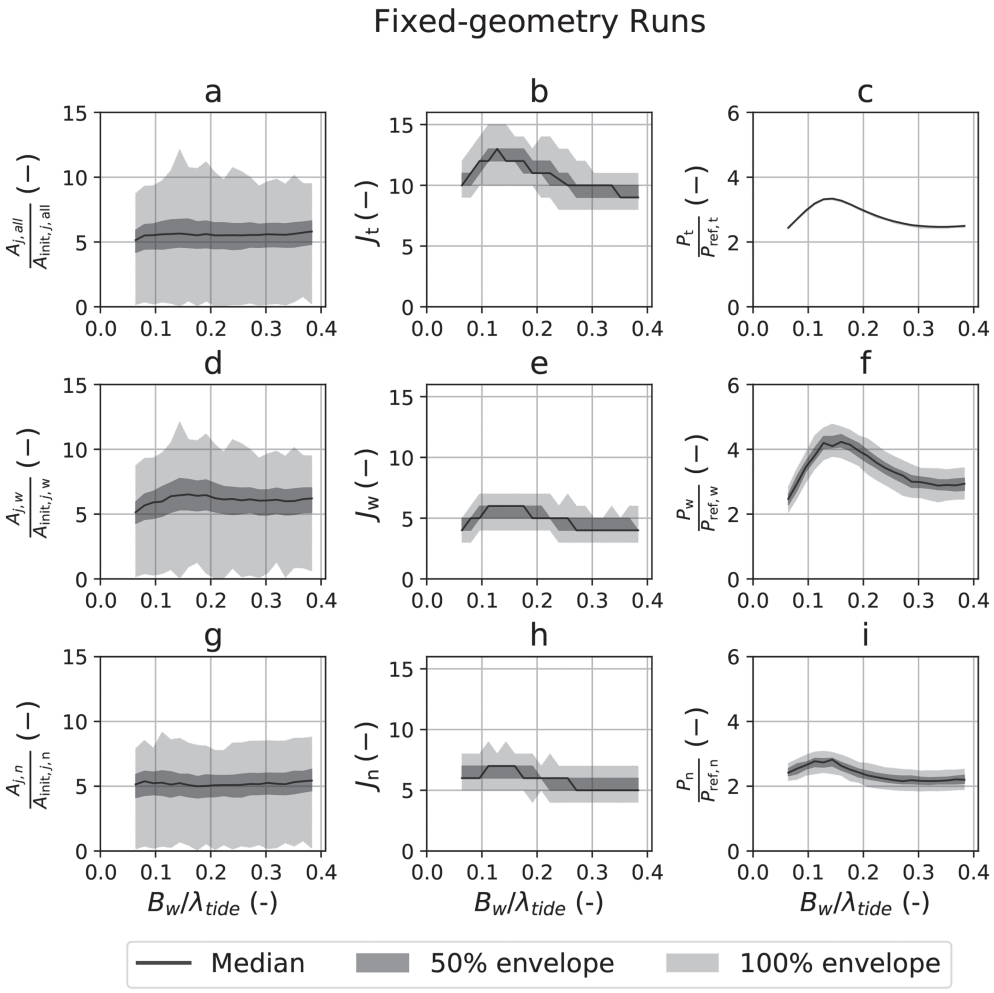

Figure 6. Results of end states of the fixed-geometry runs to identify the effect of basin size on the cross-section A_j of each open inlet in all simulations, the number of inlets J, and the tidal prism P summed over all inlets. The relative inlet cross-section $A_j/A_{\text{init},j}$ for each open inlet is shown for (a) the total basin ($A_{j,\text{all}}/A_{\text{init},j,\text{all}}$); (d) the wide part of the basin ($A_{j,\text{w}}/A_{\text{init},j,\text{w}}$); (g) and the narrow part of the basin ($A_{j,\text{n}}/A_{\text{init},j,\text{n}}$). Similarly, the number of open inlets J and the dimensionless total tidal prism (P/P_{ref}) are shown in panels (b) and (c), for the total basin($P_\text{t}/P_{\text{ref,t}}$); (e) and (f), for the wide part of the basin ($P_\text{w}/P_{\text{ref,w}}$); (h) and (i), for and the narrow part of the basin ($P_\text{n}/P_{\text{ref,n}}$). The basin size A_{basin} was varied by varying the (cross-shore) basin width in the wide part of the basin B_w and is plotted as a fraction of the frictionless tidal wave length λ_{tide}. The median of the ensembles ($n = 100$ model runs) is shown as a solid line, the envelopes around 50% and 100% of the model runs are transparent.

the simulation period. Finally, the third panel shows that the equilibrium tidal prism approaches its equilibrium faster than the inlet cross section and number of inlets. This indicates that it reaches its equilibrium despite the individual inlets not having reached their equilibrium.

The same three metrics are shown for the equilibrium or end states of the fixed-geometry runs in Figure 6: for all inlets j, all in the entire basin (panels a–c), the inlets j, w in the wide part of the basin (panels d–f), and the inlets j, n in the narrow part of the basin (panels g–i). Our results show that the inlets in all parts of the basin are affected by the changes in basin size. For larger basin sizes up to $B_\text{w}/\lambda_{\text{tide}} = 0.15$ (with λ_{tide} the wavenumber of the tide without friction), both the number of inlets along the back-barrier basin J_t and the total tidal prism P_t increase , with a maximum for $B_\text{w}/\lambda_{\text{tide}}$%0.15. For even larger basins, both J and P decrease again until both aggregated variables reach a constant value. These results also show a large spread in inlet cross-section $A_{j,\text{all}}$ for given basin geometry, which remains more or less constant for different basin geometries. Only the cross sections of inlets in the wide part of the basin (where the width is varied) weakly respond to variations in basin geometry, as they tend to become larger than those in the narrow part of the basin (where the width is not varied).

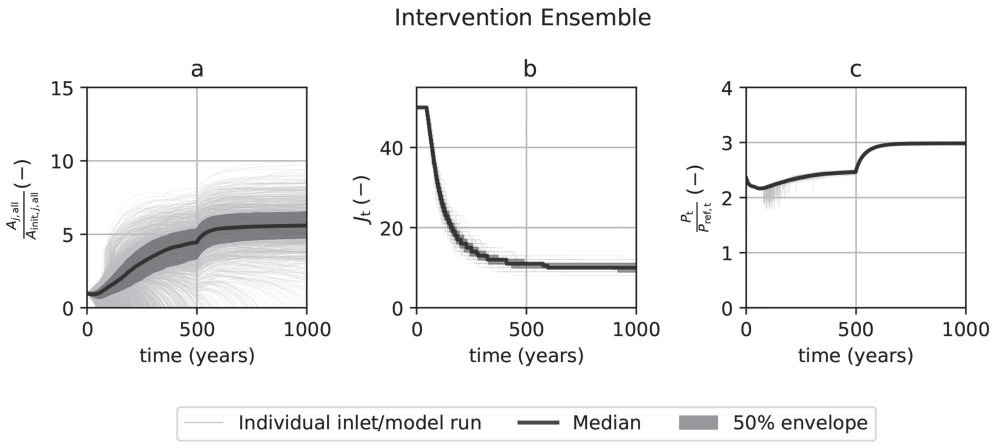

Figure 7. Same as Figure 5 but now showing the results of an intervention run, see section 2.3.2.

3.3. Intervention Runs

For a single ensemble experiment from the intervention runs (corresponding to the basin of the example run where, at $t = 500$ year, the basin width B_w is reduced from 120 to 30 km), the temporal evolution is shown in Figure 7. The temporal evolution clearly shows that the system reaches an approximate equilibrium after 500 years; after the intervention, the system is no longer in equilibrium anymore and evolves to a new equilibrium. This is reflected in both the relative inlet size of all open inlets $A_{j,\mathrm{all}}/A_{\mathrm{init},j,\mathrm{all}}$ and the dimensionless tidal prism $P_t/P_{\mathrm{ref},t}$. The only metric that appears to be unaffected is the number of inlets J_t.

The same three metrics are shown for the end states of the intervention runs in Figure 8; for the total basin (panels a–c), the wide part of the basin (panels d–f), and the narrow part of the basin (panels g–i). Similar to the fixed-geometry runs results we plotted the median, the 50% envelope, and the 100% envelope. The end states of the intervention runs show the same results for the total tidal prism P_t as the fixed-geometry runs for the same value of $B_w/\lambda_{\mathrm{tide}}$, but the results for the inlet cross-section $A_{j,\mathrm{all}}$ and number of inlets J_t are different. The effect of reducing the basin width after an equilibrium has been reached is that after the intervention the number of inlets hardly varies, primarily the size of the inlets varies to compensate for a different equilibrium tidal prism. These results are discussed further in section 4.3.

4. Discussion

4.1. The Effect of Basin Area on Tidal Prism

Our results for the total tidal prism P_t (panel c in Figures 6 and 8) show that for a multiple inlet system the tidal prism is predominantly determined by the overall basin area A_{basin} and much less by variations in (initial) inlet characteristics, as can be seen by the overlapping of the median and 50% and 100% envelopes. Further evidence for this comes from the fact that the total tidal prism for the entire basin is the same for the fixed-geometry runs and the intervention runs, implying that it is unaffected by the initial conditions of the tidal inlets. This also implies that the variations in the total tidal prism in the wide and narrow part of the basin are mostly due to variations in the equilibrium configuration of the tidal inlets.

Thus, the equilibrium configuration of the tidal inlets adapts to convey the total tidal prism P_t. This helps explaining the variations in tidal prism in the (unaltered) narrow part of the basin due to variations in (cross-shore) basin width in the wide part of the basin. The basin area determines the equilibrium tidal prism P_t of the system, so variations in basin area will lead to variations in P_t. In turn, the tidal inlets in the entire basin will evolve (due to inlet interaction) such that in their equilibrium configuration the entire tidal prism is conveyed by them.

For single inlet systems, the tidal prism has been observed to satisfy a linear relation with basin area (e.g., O'Brien, 1931), that is, a *linear regime*, sometimes referred to as a *pumping mode*. This observation was also used for modeling these systems (e.g., van de Kreeke, 1990; 1990; Van Goor et al., 2003; D'Alpaos et al., 2010; Brouwer et al., 2012). Our results for multiple inlet systems only support the occurrence of linear regimes in short basins (i.e., $B \ll \lambda_{\mathrm{tide}}$) but clearly indicate that this observation does not hold in longer basins where resonance can occur. Two additional regimes can be identified besides the classic linear regime, in

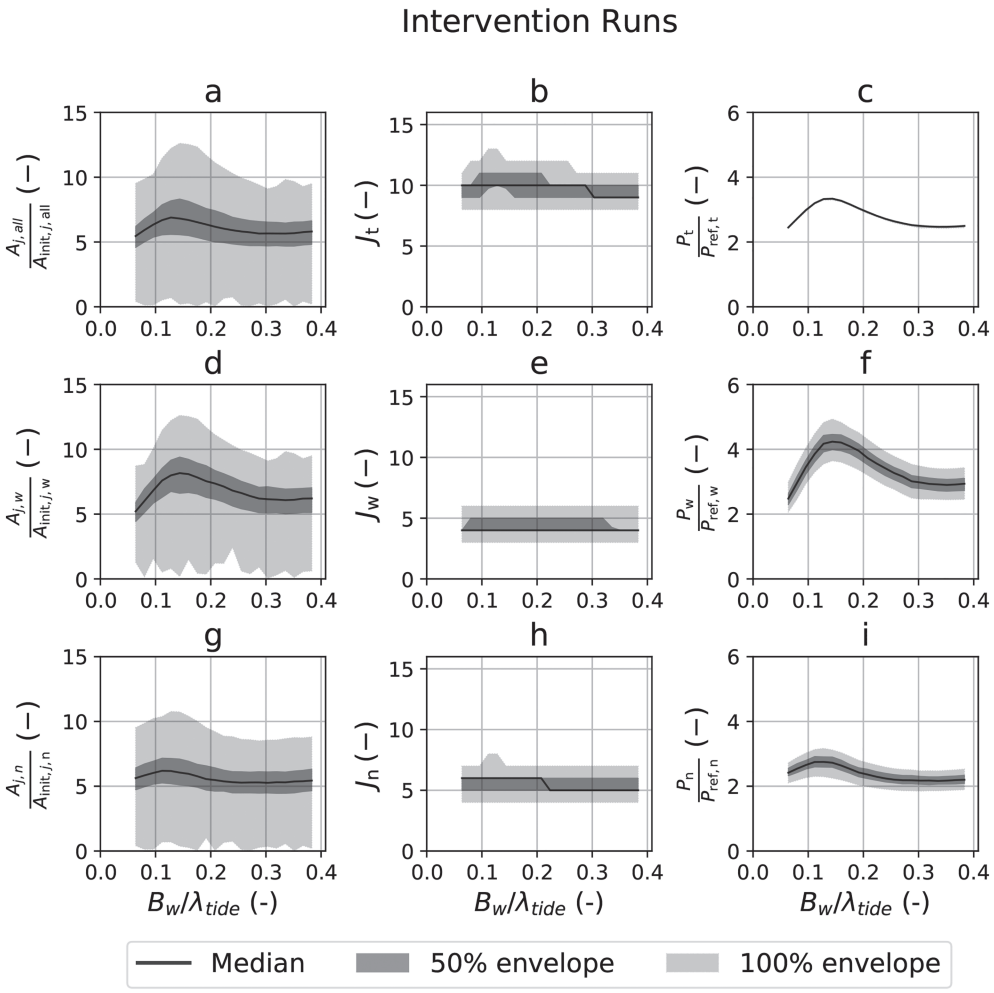

Figure 8. Same as Figure 6 but now showing the results of the intervention runs, see section 2.3.2.

our results on multiple inlet systems. First, a clear maximum can be seen in the total tidal prism P_t, implying a resonant regime. Second, the total tidal prism P_t becomes invariant for ever larger basins, implying a dissipative regime. In the next subsection these observations and the processes causing them are further discussed.

4.2. The Effect of Resonance and Bottom Friction on Tidal Prism

Our results show that the total tidal prism P_t (panel c in Figures 6 and 8) increases for an increase in basin width and then decreases for large enough values of B_w/λ_{tide} eventually reaching a constant value, where λ_{tide} is the wavelength of the frictionless tidal wave. The relative width of the basin at which this peak happens is $B_w/\lambda_{tide} = 0.15$. This suggests that this behavior is due to the well-known quarter wavelength resonance even though the maximum is found for $B_w/\lambda_{tide} < 0.25$.

To further investigate the importance of resonance, we used a 1D analytical model to study the effect of basin width B on the equilibrium cross section $A_{j,all}$ of a single tidal inlet connected to a rectangular basin (see Figure 9a and Appendix C). This model is forced by a tidal elevation amplitude at the seaside of the inlet (neglecting other seaside processes as Coriolis and radiative damping) and is again based on the linearized shallow water equations with a linearized friction coefficient. Using this model we compute for which inlet cross-section A_j the inlet velocity is exactly equal to the equilibrium velocity (i.e., $U = U_{eq}$). Our results in Figure 9b show that a clear resonance peak is present at $B/\lambda_{tide} = 0.25$ in case no bottom friction is present (i.e., $r_b = 0$). Stronger bottom friction (i.e., a higher value of r_b) leads to a shift of this peak toward narrower basins and a reduction of the peak. For larger basins, a constant value for the inlet cross section A_j is obtained, if bottom friction is sufficiently strong.

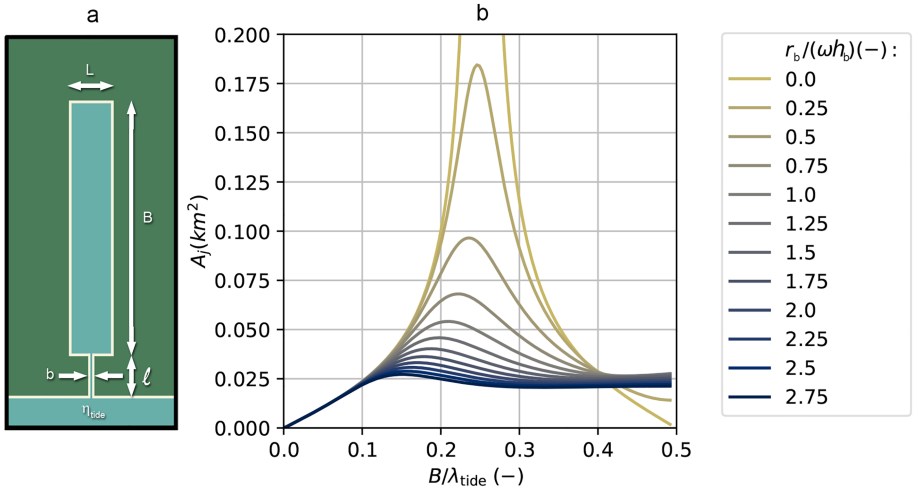

Figure 9. (a) Model geometry for our 1D model to study the effect of resonance and bottom friction on the equilibrium cross section A_j of a single tidal inlet. (b) Results of our 1D model showing different resonant responses in the inlet cross-section A_j for different (cross-shore) basin widths B/λ_{tide} and different values of the dimensionless friction coefficient $r_b/(\omega H)$. Note that λ_{tide} refers to the tidal wavelength without friction.

In narrow basins (i.e., $B \ll \lambda_{tide}$) resonance behavior does not occur, and the increase in inlet cross section depends linearly on basin area, also referred to as linear regime, see Figure 9b. Our results show that this linear regime gives way to a resonant regime around $B/\lambda_{tide} = 0.1$ or $B \sim 31$ km for the parameters in this study, although it will be lower for higher values of r_b.

Thus, the relation between basin size and tidal prism is no longer fully linear (as observed for single inlet systems; e.g., O'Brien, 1931), if the basin is sufficiently wide.

For wider basins with sufficient friction, the resonant regime gives way to a dissipative regime with constant inlet cross section A_j for increasing basin widths. Strong bottom friction causes the inlet cross-section A_j to reach a constant value with only a small resonance peak; weak bottom friction leads to a distinct resonance peak, before also reaching a constant value. This implies that the tidal wave completely dissipates in the basin and that increasing the basin width further has no effect on the water motion inside the basin and hence on the inlet cross section. Thus, a very wide basin can be accompanied by few/small tidal inlets, as can be observed in the wide and shallow Pamlico Sound behind the Outer Banks of North Carolina, USA (e.g., Inman & Dolan, 1989; Luettich et al., 2002).

4.3. The Effect of Basin Reduction

If a basin reduction is implemented, the geometry of the basin changes, and thus, the total tidal prism P_t will change as well. The results from our intervention runs (see Figure 8) show that the equilibrium configuration of the inlets indeed adapts to the new basin geometry, and a new equilibrium total tidal prism is reached that is not noticeable different from that reached in the fixed-geometry runs for the same basin geometry. However, because only a limited number of inlets are open when the basin geometry is changedf the change in tidal prism has to be accommodated by changes in the inlet cross sections. This closely mimics the situation in most barrier coast systems that are actively managed. In most of these systems new inlets are not allowed to open.

This implies that a significant reduction of basin width could lead to a regime shift from a constant to resonant regime or from a resonant to a linear regime. Thus, a decrease in basin width could lead to an increase in tidal prism and inlet cross sections. This has indeed been observed in the Western Dutch Wadden Sea, where a large bay (the former Zuiderzee) was separated from the main basin by a dam, resulting in a basin width reduction from ~115 to ~30 km. The tidal inlets in the wide part of the basin grew in size because the basin width moved closer to a resonant state (e.g., Elias et al., 2012).

4.4. Model Validity and Limitations

To assess the performance of our model we compare the model results with the real-word systems that inspired our domain and parameter choices: the Wadden Sea and Pamlico Sound. Comparison of the example runs with the real-world systems (see section 3.1) revealed that our model is capable of qualitatively reproducing observed phenomena. Our fixed-geometry runs (section 3.2) show that for basins narrower than the resonant condition (i.e., $B_w \ll \lambda_{tide}$) a larger basin generally corresponds to more and larger inlets (per km barrier coast), agreeing with observations (Davis & Hayes, 1984; Stutz & Pilkey, 2011). Furthermore, our intervention runs (section 3.3) agree with observations from the Western Dutch Wadden Sea. Closure of a large bay significantly reduced the basin width from $B_w \approx 0.4\lambda_{tide}$ to $B_w \approx 0.1\lambda_{tide}$, which brings the system closer to resonance. This has led to larger inlets and an increased tidal prism (Elias et al., 2003), as shown by our model results.

By basing the evolution of tidal inlets on the stability concept of Escoffier (1940) and coupling that with an idealized hydrodynamic model accounting for tidal oscillations under the influence of bottom friction and resonance, we were able to get a good qualitative comparison between our model results and the observations. To improve this comparison, one has to extend the model by including morphological features and processes neglected in this study. Previous studies have noted the importance of morphological features such as tidal divides (van de Kreeke et al., 2008; de Swart & Volp, 2012), channel networks (Kragtwijk et al., 2004; Reef et al., 2018), ebb and flood deltas (Gerritsen et al., 2013; Elias et al., 2012), and the formation of new tidal inlets through storm-induced breaching of barrier islands (Sallenger, 2000; Kraus et al., 2002). It has also been suggested that processes such as the morphological evolution in the basin and outer sea (Kragtwijk et al., 2004; Elias et al., 2012), nonlinear hydrodynamics (Salles et al., 2005), residual transport (Duran-Matute et al., 2014; Sassi et al., 2015), and changes in boundary conditions due to climate change such as sea level rise and changes in long-shore drift (Glaeser, 1978; Stutz & Pilkey, 2011) affect the long-term evolution of barrier coast systems as well.

5. Conclusions

We studied the effect of basin geometry and (cross-shore) basin width reduction on the long-term evolution and equilibrium configuration of tidal inlets in a meso-tidal barrier coast. Our newly developed model allowed us to simulate the long-term morphological evolution, from an oversaturated state to an equilibrium state, of multiple tidal inlets connected to a back-barrier basin with a non-uniform basin width. Simulations of the Western Dutch Wadden Sea and the Pamlico Sound showed that our model was able to get results that have a good agreement with observations.

Our results display a strong relation between the basin size and the total tidal prism in the basin. However, this relation is not always linear (i.e., a linear regime) as has been observed for single inlet systems with a small tidal basin. For shorter basins, the tidal prism increases approximately linearly for an increase in basin size linear regime, but after a resonance peak at $B_w/\lambda_{tide} = 0.15$ (resonant regime) the tidal prism decreases for an increase in basin size and reaches a constant value (dissipative regime), given that bottom friction is strong enough.

Furthermore, the equilibrium configuration of tidal inlets in the entire basin is affected by the local basin geometry (and human interventions). That is for instance the case in the Wadden Sea, where the construction of the Afsluitdijk affected all inlets in the basin, also further away from the closure dam. This is caused by changes in flow patterns in the basin and outer sea, in turn affecting inlets in the entire basin. Therefore, it is necessary to consider entire multiple inlet systems, when evaluating the effects of basin geometry or land reclamation on barrier coast systems.

Appendix A : Basin and Sea Impedance Coefficients

A1. Basin Impedance Coefficients

In this subsection, we seek an expression for the basin impedance coefficients z_{b,j_s,j_a} for inlet j_a due to a flow of water in inlet j_s (see equation (18b)). First, we formulate the model equation 10b in terms of complex amplitudes $\hat{\eta}_b(x_b, y)$, the surface amplitude in the basin, and $\hat{u}_b$, the velocity amplitude in the basin defined in equation (15)

$$(^2\hat{\eta}_b + \mu_b^2 k_b^2 \hat{\eta}_b = 0, \tag{A1a}$$

$$\hat{u}_b = \frac{gi}{\mu_b^2 \omega} (\hat{\eta}_b, \tag{A1b}$$

where $\mu_b^2 = 1 - ir_b/(\omega h_b)$ is a frictional correction factor. The basin boundary conditions that describe the exchange of water with the tidal inlets and no exchange along the other parts of the basin (see equation (12)), read

$$\frac{\partial \hat{\eta}_b}{\partial x_b} = -\frac{i\mu_b^2 \omega}{g} \hat{u}_b \quad \text{at an inlet,} \tag{A2}$$

$$(\hat{\eta}_b \cdot \mathbf{n} = 0 \quad \text{at} \quad \partial\Omega. \tag{A3}$$

Here $\hat{u}_b$ is prescribed by using equation (13) for the complex amplitudes of the velocity (i.e., $h_j \hat{u}_j = h_b \langle \hat{u}_b \rangle_j$) and assuming that exchange of water between the inlet and the basin is uniformly distributed over the inlet cross-section (i.e., $h_j \hat{u}_j = h_b \hat{u}_b$). Next, an explicit solution for $\hat{\eta}_b(x_b, y)$ can be found by using the Green's function G_b (see, e.g., Sommerfeld, 1949) that describes the impact of a Dirac-type of flow over the basin boundary on the basin hydrodynamics and that solves equation (A1a) and the boundary conditions in equation (A2) and equation (A3). This solution reads

$$\hat{\eta}_b(x_b, y) = \sum_{j=1}^{J} \int_{y_{j_s} - b_{j_s}/2}^{y_{j_s} + b_{j_s}/2} \hat{u}_b(0, y_s) G_b(x_b, y; 0, y_s) \mathrm{d}y_s, \tag{A4}$$

with x_s and y_s being the coordinates where the boundary condition in equation (A2) is applied. The influence of one inlet on $\hat{\eta}_b(x_b, y)$ denoted by $\hat{\eta}_{b,j_s}(x_b, y)$ is given by

$$\hat{\eta}_{b,j_s}(x_b, y) = \int_{y_{j_s} - b_{j_s}/2}^{y_{j_s} + b_{j_s}/2} \hat{u}_b(0, y_s) G_b(x_b, y; 0, y_s) \mathrm{d}y_s, \tag{A5}$$

where Green's function G_b associated with equation (A1a) and the boundary conditions in equations (A2) and (A3) is given by (e.g., Sommerfeld, 1949; Polyanin, 2002)

$$G_b(x_b, y; x_s, y_s) = \frac{\omega \mu_b^2}{gi} \sum_{m=0}^{\infty} \frac{\psi_m(x_s, y_s) \psi_m(x_b, y)}{(\lambda_m - \lambda) ||\psi_m||^2}, \tag{A6}$$

with ψ_m the eigenfunctions for a closed basin, $||...||^2$ the L^2-norm, $\lambda = \mu_b^2 k_b^2$, and λ_m the eigenvalue associated with ψ_m. Here we assume $\lambda \neq \lambda_m$. For cases with friction, this is always the case since λ has an imaginary part and λ_m does not.

By averaging $\hat{\eta}_{b,j_s}$ over action inlet j_a and applying the matching condition in equation (13), we obtain an expression for the basin impedance z_{b,j_s,j_a} as defined in equation (18b) by

$$\langle \hat{\eta}_{b,j_s}(0, y) \rangle_{j_a} = \left[\frac{b_{j_s} h_{j_s}}{h_b} \frac{\omega \mu_b^2}{gi} \sum_{m=0}^{\infty} \frac{\langle \psi_m(0, y_s) \rangle_{j_s} \langle \psi_m(0, y) \rangle_{j_a}}{(\lambda_m - \lambda) ||\psi_m||^2} \right] \hat{u}_{j_s} \qquad \left(= z_{b,j_s,j_a} \hat{u}_{j_s} \right). \tag{A7}$$

More information about the numerical procedure that is used to find the eigenfunctions ψ_m and eigenvalues λ_m is given in Appendix B.

A2. Sea Impedance Coefficients

We seek an expression for the sea impedance coefficients z_{o,j_s,j_a} for inlet j_a due to a flow of water in inlet j_s (see equation (18a)). First, we formulate the model equation (8b) in terms of complex amplitudes $\hat{\eta}_o(x_o, y)$, the surface amplitude in the outer sea, and $\hat{u}_o$, the velocity amplitude in the outer sea defined in equation (14)

$$(^2 \hat{\eta}_o + k_o^2 \hat{\eta}_o = 0, \tag{A8a}$$

$$\hat{u}_o = \frac{gi}{\omega} (\hat{\eta}_o, \tag{A8b}$$

with $k_o = \omega/\sqrt{gh_o}$ the shallow water wave number and $\hat{u}_o = (\hat{u}_o, \hat{v}_o)$ with $\hat{u}_o$ the velocity component in x-direction and $\hat{v}_o$ the velocity component in y-direction.

At the coastal boundary where no inlets are present, we require the normal velocity to vanish. This implies

$$\hat{u}_o = 0 \text{ so } \frac{\partial \hat{\eta}_o}{\partial x} = 0, \quad \text{at} \quad \partial\Omega, \tag{A9}$$

with $\partial\Omega$ the coastline where no inlets are present. At the tidal inlets we require the transport of water through each inlet j to match the transport of water in the adjacent sea, that is

$$h_o \langle u_o \rangle_j = h_j u_j, \tag{A10}$$

where the angle brackets again denote averaging over the width of a tidal inlet. Next, we consider the Green's function for the elevation amplitude contribution $\hat{\eta}_{o,j_s}$ in the outer sea that describes the impact of a Dirac-type of flow of water over the sea boundary at inlet j_s

$$\hat{\eta}_{o,j_s}(x_o, y) = \int_{y_{j_s}-b_{j_s}/2}^{y_{j_s}+b_{j_s}/2} \hat{u}_o(0 y_s) G_o(x_o, y; 0, y_s) \mathrm{d}y_s, \tag{A11}$$

where we use the oceanic Green's function G_o given by Buchwald (1971) but without the Coriolis effect ($f = 0$). This Green's function describes the impact of a flow through the inlets over the outer sea boundary on the outer sea hydrodynamics and that solves equation (A8a) with boundary conditions (equations (A9) and (A10)). This solution reads

$$G_o(x_o, y; 0, y_s) = \frac{\omega}{2g} H_0^{(2)}(k_o d), \tag{A12}$$

with $H_0^{(2)}$ being the Hankel function of the second kind of order zero and $d = \sqrt{(x_o - x_s)^2 + (y - y_s)^2}$ the distance from inlet j_s.

Finally, we average $\hat{\eta}_{o,j_s}(x_o, y)$ over action inlets j_a and apply the matching condition in equation (A10) to achieve an expression for the sea impedance z_{o,j_s,j_a} as in equation (18a)

$$\begin{aligned}
\langle \hat{\eta}_{o,j_s}(x_o, y) \rangle_{j_a} = \frac{h_{j_s} \omega b_{j_a}}{2gh_o} \Bigg[& \beta_{j_s,j_a} + \frac{2\mathrm{i}}{\pi} \Bigg(\beta_{j_s,j_a} \frac{3}{2} - \beta_{j_s,j_a} \Gamma \\
& - \beta^{\oplus 2}_{j_s,j_a} \ln \frac{1}{2} k_o b_{j_a} \sqrt{\alpha^2_{j_s,j_a} - \beta^{\oplus 2}_{j_s,j_a}} \\
& + \beta^{\ominus 2}_{j_s,j_a} \ln \frac{1}{2} k_o b_{j_a} \sqrt{\alpha^2_{j_s,j_a} - \beta^{\ominus 2}_{j_s,j_a}} \\
& + \alpha_{j_s,j_a} \left\{ \beta^{\ominus}_{j_s,j_a} \ln \frac{\alpha_{j_s,j_a} + \beta^{\ominus}_{j_s,j_a}}{\alpha_{j_s,j_a} - \beta^{\ominus}_{j_s,j_a}} - \beta^{\oplus}_{j_s,j_a} \ln \frac{\alpha_{j_s,j_a} + \beta^{\oplus}_{j_s,j_a}}{\alpha_{j_s,j_a} - \beta^{\oplus}_{j_s,j_a}} \right\} \\
& + \alpha^2_{j_s,j_a} \ln \sqrt{\frac{\alpha^2_{j_s,j_a} - \beta^{\ominus 2}_{j_s,j_a}}{\alpha^2_{j_s,j_a} - \beta^{\oplus 2}_{j_s,j_a}}} \Bigg] \Bigg] \hat{u}_{j_s} \qquad (= z_{o,j_s,j_a} \hat{u}_{j_s}),
\end{aligned} \tag{A13}$$

with $\beta_{j_s,j_a} = b_{j_s}/b_{j_a}$, $\alpha_{j_s,j_a} = |y_{j_a} - y_{j_s}|/b_{j_a}$, $\beta^{\oplus}_{j_s,j_a} = (\beta_{j_s,j_a} + 1)/2$, $\beta^{\ominus}_{j_s,j_a} = (\beta_{j_s,j_a} - 1)/2$, and $\Gamma = 0.57721...$ being Euler's constant. The inequality $\alpha_{j_s,j_a} > \beta^{\oplus}_{j_s,j_a}$ is satisfied since the inlets are separated by a finite distance.

The above expression concerns the cross-impedance, (i.e., $j_s \neq j_a$), the self-impedance (i.e., $j_s = j_a$) is given by

$$\langle \hat{\eta}_{o j_s}(x_o, y) \rangle_{j_s} = \frac{h_{j_s} \omega b_{j_s}}{2gh_o} \left[1 + \frac{2\mathrm{i}}{\pi} \left(\frac{3}{2} - \Gamma - \ln \frac{k_o b_s}{2} \right) \right] \hat{u}_{j_s} \qquad (= z_{o j_s j_s} \hat{u}_{j_s}). \tag{A14}$$

Appendix B : Eigenfunctions

The eigenfunctions ψ_m in equation (A6) can be found by solving the following EigenValue Problem (EVP) with reflective boundaries

$$\nabla^2 \psi_m = -\lambda_m \psi_m, \tag{B1}$$

where λ_m are the corresponding eigenvalues. As such, there is a distinct set of eigenfunctions and corresponding eigenvalues that depends on the geometry of the basin.

For simple geometries, such as rectangular and conical basins, the eigenfunctions are easily found to be cosines and (a linear combination of) Bessel functions, respectively. For more complex geometries, as used in this study, finding the eigenfunctions and eigenvalues is not as straightforward. For a basin of arbitrarily shape, we can solve a discretized EVP of the form

$$\mathbf{A}\boldsymbol{\psi} = -\boldsymbol{\lambda}\boldsymbol{\psi}, \tag{B2}$$

in which the $P \times P$ matrix $\mathbf{A}$ holds the discretized ∇^2 operator from equation (B1) on a grid of P points, $\boldsymbol{\psi}$ holds the eigenfunctions, and $\boldsymbol{\lambda}$ holds the corresponding eigenvalues.

In this study we used a second-order central difference scheme to discretize the ∇^2 operator from equation (B1) on a grid. We used a grid in which the points are spaced using $\mathrm{d}x = 100$ m in x-direction and $\mathrm{d}y = 20$ m in y-direction. The resulting grid is sufficiently fine for accurate results, while not being too computationally expensive to solve the EVP. The EVP in equation (B2) was solved using the ARPACK software library (Lehoucq et al., 1998) for finding a specified number of eigenvalues in large sparse matrices.

Appendix C : One-Dimensional Analytical Model of a Single Inlet

A one-dimensional inlet-basin model is developed to further study the effects of bottom friction and basin width on the inlet cross section. Our model consists of a narrow inlet channel that is forced by a tidal elevation η_{tide} at the seaside and is connected to a basin with no-flow boundaries. Furthermore, all seaside processes besides the forced tidal elevation are neglected (e.g., Coriolis and radiative damping).

The momentum balance in the inlet is given by equation (4). At the seaside of the inlet (i.e., at $x = -l$) a tidal elevation amplitude η_{tide} is prescribed. At the interface of the inlet and the basin, the volume transport must be equal

$$u_{\text{b}}(0,t)\, h_{\text{b}} L = u_j A_j, \tag{C1}$$

where $u_{\text{b}}(x,t)$ is the flow velocity in the basin, h_{b} the depth of the basin, L the width of the basin, u_j the flow velocity in the inlet, and A_j the inlet cross section. The model equations for the basin are given by

$$\frac{\partial u_{\text{b}}}{\partial t} + \frac{r_{\text{b}} u_{\text{b}}}{h_{\text{b}}} = -g \frac{\partial \eta_{\text{b}}}{\partial x}, \tag{C2a}$$

$$\frac{\partial \eta_{\text{b}}}{\partial t} + h_{\text{b}} \frac{\partial u_{\text{b}}}{\partial x} = 0, \tag{C2b}$$

with r_{b} the linearized friction coefficient in the basin and $\eta_{\text{b}}(x,t)$ the water level in the basin. At the closed boundaries of the basin, the normal flow must vanish. Since our 1D model only has a flow of water in the x-direction, the boundary condition at the closed end of the basin becomes

$$u_b(B,t) = 0. \tag{C3}$$

Next, we formulate the model equations in terms of complex amplitudes $(Z, \hat{\mathrm{u}}_j, \hat{\eta}_{\text{b}}, \hat{\mathrm{u}}_{\text{b}})$ using

$$(\eta_{\text{tide}}, u_j, \eta_{\text{b}}, u_{\text{b}}) = \Re\left\{(Z, \hat{\mathrm{u}}_j, \hat{\eta}_{\text{b}}, \hat{\mathrm{u}}_{\text{b}}) \exp(\mathrm{i}\omega t)\right\}, \tag{C4}$$

where ω is again the tidal frequency. The momentum equation in the inlet now becomes

$$\left[\mathrm{i}\omega + \frac{r_{\text{j}}}{h_{\text{j}}}\right] \hat{\mathrm{u}}_j = -\frac{g}{l_j}(Z - \hat{\eta}_b(0)). \tag{C5}$$

And the model equations in the basin become

$$\frac{\partial^2 \hat{u}_b}{\partial x^2} + \mu_b^2 k_b^2 \hat{u}_b = 0, \tag{C6a}$$

$$\hat{\eta}_b = \frac{i h_b}{\omega} \frac{\partial \hat{u}_b}{\partial x}. \tag{C6b}$$

By applying the boundary conditions (equations (C1) and (C3)), the solution in the basin is found to be

$$\hat{u}_b(x) = \left[-\frac{A_j u_j}{A_b \sin\left(\mu_b k_b B\right)} \right] \sin\left(\mu_b k_b [x - B]\right), \tag{C7}$$

$$\hat{\eta}_b(x) = \frac{i h_b}{\omega} \left[-\frac{A_j u_j}{A_b \sin\left(\mu_b k_b B\right)} \right] \mu_b k_b \cos\left(\mu_b k_b [x - B]\right). \tag{C8}$$

By combining equation (C5) and the solution for $\hat{\eta}_b$ at $x = 0$, we find the following expression for A_j

$$A_j = A_b \left[-\frac{\mu_j^2 k_b l_j}{\mu_b} + \frac{i\omega Z}{h_b \mu_b k_b \hat{u}_j} \right] \tan\left(\mu_b k_b B\right). \tag{C9}$$

Here, $\mu_j^2 = \left(1 - \frac{i r_j}{\omega h_j}\right)$ is a frictional correction factor that depends on the depth of the inlet, and thus on the inlet cross section (using equation ((1)). Since both sides of equation (C9) thus depend on A_j we use an iterative underrelaxation procedure to find the inlet cross section for given parameters, basin length $L = 5$ km), and requiring the inlet velocity amplitude to equal 1 m s^{-1}. We use the Wadden Sea parameters (see Table 1) and a basin of length $L = 5$ km (i.e., along-shore) and a varying width B from 0 to 155 km (i.e., cross-shore).

Acknowledgments
This research was carried out within the WADSnext! project, funded by the 'Simon Stevin Meester' prize (awarded by NWO to S.J.M.H. Hulscher), Deltares, and the 4TU centre for Fluids and Solid Mechanics. The model developed for this study is available online (Reef et al., 2019). We thank three reviewers (two anonymous and Brad Murray) for their helpful comments.

References

Brouwer, R. L., Schuttelaars, H. M., & Roos, P. C. (2012). Influence of basin geometry on equilibrium and stability of double inlet systems. In *Jubilee Conference Proceedings NCK-days 2012: Crossing borders in coastal research* (pp. 85–89).

Brouwer, R. L., Schuttelaars, H. M., & Roos, P. C. (2013). Modelling the influence of spatially varying hydrodynamics on the cross-sectional stability of double inlet systems. *Ocean Dynamics*, *63*(11-12), 1263–1278.

Buchwald, V. T. (1971). The diffraction of tides by a narrow channel. *Journal of Fluid Mechanics*, *46*(3), 501–511.

D'Alpaos, A., Lanzoni, S., Marani, M., & Rinaldo, A. (2010). On the tidal prism-channel area relations. *Journal of Geophysical Research*, *115*(1), 1–13. https://doi.org/10.1029/2008JF001243

Dastgheib, A., Roelvink, J. A., & Wang, Z. B. (2008). Long-term process-based morphological modeling of the Marsdiep Tidal Basin. *Marine Geology*, *256*(1-4), 90–100.

Davis, R. A., & Hayes, M. O. (1984). What is a wave-dominated coast? *Developments in Sedimentology*, *39*(C), 313–329.

de Haas, T., Pierik, H. J., van der Spek, A. J. F., Cohen, K. M., van Maanen, B., & Kleinhans, M. G. (2018). Holocene evolution of tidal systems in the Netherlands: Effects of rivers, coastal boundary conditions, eco-engineering species, inherited relief and human interference. *Earth-Science Reviews*, *177*(2016), 139–163. https://doi.org/10.1016/j.earscirev.2017.10.006

de Swart, H. E., & Volp, N. D. (2012). Effects of hypsometry on the morphodynamic stability of single and multiple tidal inlet systems. *Journal of Sea Research*, *74*, 35–44.

de Swart, H. E., & Zimmerman, J. T. F. (2009). Morphodynamics of tidal inlet systems. *Annual Review of Fluid Mechanics*, *41*(1), 203–229.

Duran-Matute, M., Gerkema, T., De Boer, G. J., Nauw, J. J., & Gräwe, U. (2014). Residual circulation and freshwater transport in the Dutch Wadden Sea: A numerical modelling study. *Ocean Science*, *10*(4), 611–632.

Elias, E. P. L., Stive, M., Bonekamp, H., & Cleveringa, J. (2003). Tidal inlet dynamics in response to human intervention. *Coastal Engineering Journal*, *45*(4), 629–658. http://www.worldscientific.com/doi/abs/10.1142/S0578563403000932

Elias, E. P. L., Van Der Spek, A. J. F., Wang, Z. B., & De Ronde, J. (2012). Morphodynamic development and sediment budget of the Dutch Wadden Sea over the last century. *Geologie en Mijnbouw/Netherlands Journal of Geosciences*, *91*(3), 293–310.

Escoffier, E. F. (1940). The stability of tidal inlets. *Shore and Beach*, *8*(4), 114–115.

Gerritsen, F., Dunsbergen, D. W., & Gerritsenf, F. (2013). Modelling morphological-empirical relationships for Ebb tidal deltas as a tool in dynamic-empirical modelling.

Glaeser, J. D. (1978). Global distribution of barrier islands in terms of tectonic setting. *The Journal of Geology*, *86*(3), 283–297.

Google Earth (2016). Google Earth, map data: Landsat/Copernicus. Western Dutch Wadden Sea 53°15′08.18″N, 5°10′54.56″, elevation 0m.

Inman, D. L., & Dolan, R. (1989). The Outer Banks of North Carolina: Budget of sediment and inlet dynamics along a migrating barrier system. *Journal of Coastal Research*, *5*(2), 193–237.

Jarret, J. T. (1976). Tidal prism-inlet area relationships general investigation of tidal inlets: U.S. Army Coastal Engineering Research Center, Fort Belvoir, VA. U.S. Army Engineers Waterways Experiment Station, Vicksburg, MS.

Kragtwijk, N. G., Zitman, T. J., Stive, M. J. F., & Wang, Z. B. (2004). Morphological response of tidal basins to human interventions. *Coastal Engineering*, *51*(3), 207–221.

Kraus, N. C., Militello, A., & Todoroff, G. (2002). Barrier beaching processes and barrier spit breach, Stone Lagoon, California. *Shore and Beach*, *70*(4), 21–28.

Lehoucq, R. B., Sorensen, D. C., & Yang, C. (1998). ARPACK users' guide: Solution of large-scale eigenvalue problems with implicitly restarted Arnoldi methods.

Lorentz, H. A. (1922). Ein Rechnungsansatz für den Widerstand bei Flüssigkeitsschwingungen. *De Ingenieur*, *37*, 695.

Luettich, R. A., Carr, S. D., Reynolds-Fleming, J. V., Fulcher, C. W., & McNinch, J. E. (2002). Semi-diurnal seiching in a shallow, micro-tidal lagoonal estuary. *Continental Shelf Research*, *22*(11-13), 1669–1681.

Mallinson, D., Culver, S., Leorri, E., Mitra, S., Mulligan, R., & Riggs, S. (2018). Barrier Island and Estuary Co-evolution in Response to Holocene Climate and Sea-Level Change: Pamlico Sound and the Outer Banks Barrier Islands, North Carolina, USA. In L. Moore & A. Murray (Eds.), *Barrier Dynamics and Response to Changing Climate*. Cham: Springer. https://doi.org/10.1007/978-3-319-68086-6_3

Nahon, A., Bertin, X., Fortunato, AndréB, & Oliveira, A. (2012). Process-based 2DH morphodynamic modeling of tidal inlets: A comparison with empirical classifications and theories. *Marine Geology*, *291-294*, 1–11.

National Oceanic and Atmospheric Administration (2020). NOAA tides & currents. USCG Station Hatteras, NC. https://tidesandcurrents.noaa.gov/stationhome.html?id=8654467

O'Brien, M. P. (1931). Estuary tidal prisms related to entrance areas. *Civil Engineering*, *1*(8), 738–139.

O'Brien, M. P. (1969). Equilibrium flow areas of tidal inlets on sandy coasts. *ASCE Journal of Waterways Harbors Division*, *95*, 43–52.

Oost, A. P., Hoekstra, P., Wiersma, A., Flemming, B., Lammerts, E. J., Pejrup, M., et al. (2012). Barrier island management: Lessons from the past and directions for the future. *Ocean and Coastal Management*, *68*, 18–38.

Polyanin, A. D. (2002). Handbook of linear partial differential equations for engineers and scientists.

Reef, K. R. G., Lipari, G., Roos, P. C., & Hulscher, S. J. M. H. (2018). Time-varying storm surges on Lorentz's Wadden Sea networks. *Ocean Dynamics*, *68*(8), 1051–1065.

Reef, K. R. G., Roos, P. C., Schuttelaars, H. M., & Hulscher, S. J. M. H. (2019). Free form basin model. https://zenodo.org/badge/latestdoi/214427772

Roos, P. C., Schuttelaars, H. M., & Brouwer, R. L. (2013). Observations of barrier island length explained using an exploratory morphodynamic model. *Geophysical Research Letters*, *40*, 4338–4343. https://doi.org/10.1002/grl.50843

Sallenger, A. H. (2000). Storm impact scale for barrier islands. *Journal of Coastal Research*, *16*(3), 890–895.

Salles, P., Voulgaris, G., & Aubrey, D. G. (2005). Contribution of nonlinear mechanisms in the persistence of multiple tidal inlet systems. *Estuarine, Coastal and Shelf Science*, *65*(3), 475–491.

Sassi, M., Duran-Matute, M., van Kessel, T., & Gerkema, T. (2015). Variability of residual fluxes of suspended sediment in a multiple tidal-inlet system: The Dutch Wadden Sea. *Ocean Dynamics*, *65*(9-10), 1321–1333.

Sommerfeld, A. (1949). *Partial differential equations in physics* (1st ed.). New York: Academic Press Inc.

State Committee on the Zuiderzee (1926). Report of the State Committee on the Zuiderzee (in Dutch). 's Gravenhage: Algemene Landsdrukkerij.

Stutz, M. L., & Pilkey, O. H. (2011). Open-ocean barrier islands: Global influence of climatic, oceanographic, and depositional settings. *Journal of Coastal Research*, *27*(2), 207–222.

Tran, T.-T., van de Kreeke, J., Stive, MarcelJ. F., & Walstra, Dirk-JanR. (2012). Cross-sectional stability of tidal inlets: A comparison between numerical and empirical approaches. *Coastal Engineering*, *60*, 21–29.

United States Geological Survery (2019). National Water Information System: Web interface. USGS 02084472 PAMLICO RIVER AT WASHINGTON, NC. waterdata.usgs.gov

Van Goor, M. A., Zitman, T. J., Wang, Z. B., & Stive, M. J. F. (2003). Impact of sea-level rise on the morphological equilibrium state of tidal inlets. *Marine Geology*, *202*(3-4), 211–227.

van de Kreeke, J. (1990). Can multiple tidal inlets be stable? *Estuarine, Coastal and Shelf Science*, *30*(3), 261–273.

van de Kreeke, J. (1990). Stability analysis of a two-inlet bay system. *Coastal Engineering*, *14*(6), 481–497.

van de Kreeke, J. (2004). Equilibrium and cross-sectional stability of tidal inlets: Application to the Frisian inlet before and after basin reduction. *Coastal Engineering*, *51*(5-6), 337–350.

van de Kreeke, J., Brouwer, R. L., Zitman, T. J., & Schuttelaars, H. M. (2008). The effect of a topographic high on the morphological stability of a two-inlet bay system. *Coastal Engineering*, *55*(4), 319–332.

Vos, P. C., & Knol, E. (2015). Holocene landscape reconstruction of the Wadden Sea area between Marsdiep and Weser. *Geologie en Mijnbouw/Netherlands Journal of Geosciences*, *94*(2), 157–183.

Wang, Z. B., Hoekstra, P., Burchard, H., Ridderinkhof, H., De Swart, H. E., & Stive, M. J. F. (2012). Morphodynamics of the Wadden Sea and its barrier island system. *Ocean & Coastal Management*, *68*, 39–57.